Heliyon 12 (2026) e45716

Contents lists available at ScienceDirect

Heliyon

journal homepage: www.cell.com/heliyon

Research article

Tailoring turbulence promoter geometry and material to enhance hydrodynamics and mitigate fouling in ultrafiltration

Aws N. Al-Tayawi [a,b,*], Zsuzsanna Horváth Hovorka [c], Orlando Castilleja-Escobedo [d], David De Haro Del Rio [d,e], José L. López-Salinas [d], Szabolcs Kertész [f]

[a] Doctoral School of Environmental Sciences, University of Szeged, Szeged, H-6725, Hungary
[b] Department of Environmental Technology, Faculty of Environmental Sciences, University of Mosul, Mosul, 41002, Iraq
[c] Department of Mechanical Engineering, Faculty of Engineering, University of Szeged, Szeged, H-6725, Hungary
[d] Tecnologico de Monterrey Escuela de Ingeniería y Ciencias, Tecnológico de Monterrey, Av. Eugenio Garza Sada 2501, Monterrey, N.L., C.P. 64849, Mexico
[e] Universidad Politécnica de Apodaca, Av. Politécnica No. 2331, Col. El Barretal, Apodaca, NL, CP 66600, Mexico
[f] Department of Biosystems Engineering, Faculty of Engineering, University of Szeged, Hungary

ARTICLE INFO

Keywords:
3D printed turbulence promoters
Flow dynamics assessment
Membrane fouling
Dairy wastewater treatment
Computational fluid dynamics

ABSTRACT

In this study, the impact of various designs and materials of turbulence promoters used to mitigate membrane fouling using dairy model wastewater in a laboratory-scale ultrafiltration unit has been studied and investigated. Membrane separation parameters were examined, including total, reversible, and irreversible resistances, membrane retention, and permeate flux. Using a transmembrane pressure of 0.3 MPa, a stirring speed of 400 rpm, and a 20 kDa polyethersulfone membrane as fixed operational parameters, various turbulence promoter designs printed with different materials were tested to determine the optimal design and material. It was found that certain turbulence promoter designs, particularly *PLA-UE* and *PLA-S*, significantly improved the average permeate fluxes and slightly enhanced *COD* retentions. Furthermore, among the different printed materials tested, the resin stood out, significantly increasing the permeate flux while reducing the total resistance. A computational fluid dynamics model was specified to analyze the effect of turbulence promoters on the hydrodynamics of the filtration system. Statistical analysis was also performed to optimize these parameters.

Abbreviations

Molecular weight cut-off [kDa]	*MWCO*
Transmembrane pressure [MPa]	*TMP*
Total resistance [m^{-1}]	R_T
Membrane resistance [m^{-1}]	R_M
Irreversible resistance [m^{-1}]	R_{IRR}
Reversible resistance [m^{-1}]	R_{REV}
Membrane surface area [m^2]	*A*
Flux [L m^{-2} h^{-1}]	*J*
Permeate volume [m^3]	*V*

(*continued on next page*)

* Corresponding author. Doctoral School of Environmental Sciences, University of Szeged, Szeged, H-6725, Hungary
E-mail address: awsaltayawi@uomosul.edu.iq (A.N. Al-Tayawi).

https://doi.org/10.1016/j.heliyon.2026.e45716
Received 2 February 2026; Received in revised form 15 September 2026; Accepted 2 November 2026
2405-8440/© 2026 The Authors. Published by Elsevier Ltd. This is an open access article under the CC BY license (http://creativecommons.org/licenses/by/4.0/).

(*continued*)

Filtration time [s]	t
Retention [%]	R
Concentration of the feed [mg L^{-1}]	C_F
Concentration of the permeate [mg L^{-1}]	C_P
Volume Reduction Ratio [−]	VRR
Membrane Water flux after filtration [L m^{-2} h^{-1}]	J_{WA}
The initial water flux before filtration [L m^{-2} h^{-1}]	J_{WB}
Water viscosity at 25°C [Pa.s]	ηw
The dynamic viscosity of wastewater at 25°C [Pa.s]	η_{ww}
The wastewater constant flux [L m^{-2} h^{-1}]	J_{ww}
Reynolds number [−]	Re
The solution density [kg m^{-3}]	ρ
Velocity [m s^{-1}]	υ
Diameter of the magnetic stirrer [m]	d
Solution's viscosity [Pa.s]	η
Total dissolved solids	*TDS*
Polyethersulfone	*PES*
Polylactic acid	*PLA*
Polyamide	*PA*
polylactic acid-unrestricted end starting	*PLA-UE*
Chemical oxygen demand	*COD*
Polylactic acid-slim	*PLA-S*
Polylactic acid-thin barrier	*PLA-TB*
Polyamide-dual barrier	*PA-DB*
Thermoplastic polyurethane	*TPU*

1. Introduction

Rapid population growth and increasing environmental pressures have emphasized the urgent need to protect natural water resources and reduce wastewater generation [1,2], Many industry participate in this issue, particularly in water-intensive sectors, such as the dairy industry, which also generates complex wastewater streams [3–5]. To address these challenges, advanced and reliable treatment technologies, especially hybrid processes, are increasingly essential [6], One of the key technologies is the membrane, with ultrafiltration emerging as a promising solution [7,8]. However, membrane applications are often hindered by fouling and concentration polarization [9,10], which reduce flux, impair rejection performance, shorten membrane life, and increase operational costs due to accumulation of particulate, organic, inorganic, and biological foulants on or within the membrane [11]. Recent advances in additive manufacturing (3D printing) offer new opportunities to mitigate these limitations by enabling the fabrication of intricate, highly customized geometries that are used to improve the hydrodynamic one the membrane surface [12–14], using a wide range of materials (most commonly thermoplastic polymers) through widely adopted technologies such as fused deposition modeling (*FDM*) [15].

The incorporation of turbulence promoters has shown significant potential to mitigate membrane fouling by improving the shear rate on the membrane surface [16–18], where the efficacy of this approach in addressing organic fouling within membrane processes has been also demonstrated [19]. In this contest, the geometry of the turbulence promoters plays a crucial role in enhancing membrane performance and decreasing the polarization of membrane fouling by optimizing the mixing and overall performance [20]. Various wastewater treatment units have adopted this approach; for example, perforated feed promoters with contamination resistance have been shown to be effective in combating organic and biological fouling on membrane surfaces [21]. Furthermore, 3D printed spacers, made by 3D printing and UV curing, exhibited fouling resistance and increased permeate flux compared to traditional commercial spacers. These integrated spacers offered flexibility, mechanical integrity and strong adhesion to the ultrafiltration membrane [22,23]. Furthermore, integration of turbulence promoters has improved filtration parameters and reduced membrane fouling in various membrane separation modules [24].

Enhancing the hydrodynamic conditions on the membrane surface is widely recognized as an effective fouling mitigation strategy that does not require alteration of membrane materials, enabling straightforward integration into commercial systems. Such enhancement is typically achieved by introducing structural features (ridges, pillars, corrugations, or spacers) that generate vortices, secondary flows, and elevated shear, thereby improving foulant back-transport and reducing concentration polarization. As reported by Qian et al. [25], research interest in turbulence promoters and spacers has grown rapidly across *UF*, *RO*, *FO*, and *MD* applications. Early work by Armbruster et al. [26] established that turbulence promoters increase shear by redirecting flow and inducing vortices, while Fodor et al. [27] demonstrated that 3D printed spacers enhance mixing and mass transfer, leading to reduced fouling. As printing technologies progress toward finer resolutions, the fabrication of application-specific hydrodynamic elements has become increasingly feasible. Recent studies provide strong evidence for the efficacy of turbulence promoters. Jiang et al. [28] showed that incorporating a turbulence promoter in nanofiltration markedly improved hydrodynamics, reduced humic acid deposition, and increased membrane lifespan by up to 85.7%.

Wu et al. [29] reported that vibrating 3-D spacers reduced fouling more effectively than 1D or 2-D designs, with performance

further enhanced by increasing vibration frequency and amplitude. CFD simulations attributed these improvements to elevated turbulence kinetic energy and shear. Cabrera Castillo et al. [30] demonstrated that 3D printed spacers increased flux by 50–65% compared to commercial spacers, with the Gyroid structure offering superior long-term fouling resistance. In cross-flow microfiltration, Tsai et al. [31] showed that elliptic promoters produced flux enhancements of 30–64%, highlighting the critical role of geometry. A recent review by Ng et al. [32] emphasized that spacer performance is strongly determined by the printing method, material properties, and geometric configuration, although the mechanistic understanding of design–hydrodynamics relationships remains incomplete and needs more investigation.

This study builds directly upon two prior investigations by our research group. Al-Tayawi et al. [33] characterized a single 3D-printed *PLA* turbulence promoter prototype, comprising a concentric-ring geometry with 18 interconnecting baffles secured by upper and lower sealing O-rings, within a 150 kDa *MWCO* stirred ultrafiltration cell operated at stirring speeds of 0-400 rpm; applying the Hermia and resistance-in-series models, that study identified cake-layer formation as the dominant fouling mechanism and demonstrated substantial flux enhancement and resistance reduction relative to an unmodified control. Szpisják-Gulyás et al. [34] extended this work using a geometrically distinct spoke-type *PLA* promoter within a 30 kDa *MWCO* cell, varying both transmembrane pressure (0.1-0.3 MPa) and stirring speed (100-400 rpm) and incorporating the Makardij model to resolve deposition and removal rate kinetics. Both studies, however, evaluated only a single, unmodified promoter geometry fabricated from a single material, leaving the combined effects of geometry and material selection, and any mechanistic hydrodynamic basis for the observed improvements, unexplored. The present study addresses this gap by directly comparing four promoter geometries with controlled variation in membrane contact area and baffle configuration, two of which (PLA-UE and PLA-S) are adapted from the designs in Refs. [33] and [34], respectively; independently evaluating four fabrication materials for the best-performing geometry; employing 20 kDa *MWCO* membrane under operating conditions adopted from an independently validated optimization study; and integrating the experimental analysis with a CFD model, including a formal mesh-independence assessment, to establish a mechanistic basis for the observed structure-hydrodynamics-performance relationships. In doing so, this work moves beyond the geometry-only or material-only optimization typical of prior crossflow-focused studies, providing a combined design-material optimization framework for turbulence promoters in stirred UF systems.

2. Materials and methods

2.1. Preparation of the dairy wastewater model

A synthetic 5 g L^{-1} effluent resembled dairy wastewater was created before each experiment (to ensure the use of a fresh dairy wastewater model). To prepare 1 L of the synthetic effluent, 5 g of skim milk powder (Tutti Kft., Hungary) and 0.5 g of anionic detergent (Chemipur Cl80, Hungaro Chemicals, Hungary) were dissolved in tap water at 25°C. Based on the body of research on the *COD* of typical dairy wastewater, these concentration limits were chosen [35]. The average measured parameters for the effluent of the model were pH 8.7, turbidity [NTU] 1150, electrical conductivity [mS cm^{-1}] 0.89, and COD [mg L^{-1}] 5200. Synthetic dairy wastewater was freshly prepared according to an identical protocol before each experiment. Although a separate batch-to-batch variability dataset was not included, repeated experiments showed consistent flux and resistance trends, indicating acceptable reproducibility of the synthetic dairy preparation method. Each experimental condition was independently repeated twice (independent experimental replicates) to ensure reproducibility. Within each experimental run, *COD* measurements used to determine membrane retention were carried out in five parallel measurements, representing technical replicates. Thus, the reported values are based on two independent experimental runs, each comprising five technical measurements. Statistical analyses were performed using TIBCO Statistica software. One-way analysis of variance (ANOVA) was used to evaluate differences between experimental conditions, including turbulence promoter designs and materials, and Fisher's Least Significant Difference (LSD) test was applied as the post hoc procedure to identify significant differences between individual groups. Prior to ANOVA, the assumptions of normality and homogeneity of variances were assessed. Differences between groups were considered statistically significant at a 95% confidence level ($p < 0.05$); the corresponding 95% confidence intervals shown in the figures were generated by the software and are based on the error variance calculated during the ANOVA analysis. Given the limited sample size ($n = 2$ independent replicates per condition), the formal assessment of normality and homogeneity of variance possesses inherently limited statistical power; accordingly, these diagnostic checks and the resulting confidence intervals should be interpreted with due caution. The statistical analysis is therefore intended primarily to characterize comparative trends among experimental conditions rather than to provide fully powered inferential conclusions.

2.2. Membrane equipment and its key parameters

An ultrafiltration stirred cell system (Merck Millipore, Germany), providing an effective membrane area of 0.0036 m^2, was used for all experiments. The operating parameters employed in the present study (20 kDa polyethersulfone (*PES*) membrane, transmembrane pressure of 0.3 MPa, and stirring speed of 400 rpm) were not optimized as part of the present work. Instead, these conditions were adopted directly from a previously published independent optimization study conducted by our group [36], accordingly, all experiments in the present work were conducted under these conditions. Transmembrane pressure was regulated using a pressure control valve connected to a nitrogen gas pressurized feed vessel. Each filtration run was continued until the feed volume was reduced from 100 mL to 50 mL, corresponding to a volume reduction ratio (*VRR*) of 2. The permeate was collected through the outlet located at the bottom plate of the cell, and the permeate mass was continuously monitored using an electronic balance (Kern EW) to determine

permeate volume and flux evolution over time.

The efficiency of a given membrane can be described by using several key parameters. Filtration speed can be measured in terms of permeate flux (Equation. (1)) [37,38]. And membrane selectivity is usually expressed in terms of retention or rejection (Equation. (2)) [39]. And lastly, the filtration efficiency can be examined in terms of resistances (Equations (3)–(7)). The hydrodynamic conditions in a membrane filtration cell were investigated by calculating the Reynolds number (*Re*) (Equation. (8)) [40].

$$J = \frac{1}{A} \cdot \frac{dV}{dt} \quad \left[L \cdot m^{-2} \cdot h^{-1}\right] \tag{1}$$

$$R = \frac{c_f - c_p}{c_f} \cdot 100\ [\%] \tag{2}$$

$$R_T = R_M + R_{IRREV} + R_{REV}\ \left[\mathrm{m}^{-1}\right] \tag{3}$$

$$R_M = \left(\frac{TMP}{J_{WB} \cdot \eta_W}\right)\ \left[\mathrm{m}^{-1}\right] \tag{4}$$

$$R_{REV} = \frac{TMP}{J_{WW} \cdot \eta_{WW}} - R_M - R_{IRREV}\left[\mathrm{m}^{-1}\right] \tag{5}$$

$$R_{IRREV} = \frac{TMP}{J_{WA} \cdot \eta_W} - R_M\ \left[\mathrm{m}^{-1}\right] \tag{6}$$

$$\%\ reduction\ R_T = \frac{\left(R_{T\,Control} - R_{T\,Sample)}\right.}{R_{T\,Control}} \times 100 \tag{7}$$

$$Re = \frac{\rho v d}{\eta} \tag{8}$$

2.3. Turbulence promoters designs and materials

Depending on the principles of fluid dynamics and by modifying the contact areas with the membrane surface, four designs of turbulence promoters were evaluated. These promoters were made from polylactic acid (*PLA*). The first design was *PLA*-Unrestricted End Start (*PLA-UE*) (Fig. 1-A) adapted from the concentric-ring turbulence promoter design reported in Ref. [33]. Whereas the original design was secured to the filtration cell using two sealing O-rings (top and bottom), the present design removes the upper O-ring, leaving the promoter constrained only at the lower ring-hence "Unrestricted End", this design incorporates two circular rings (outer diameters: 6.49 cm and 4.59 cm; width: 2 mm) that contact the membrane surface. The total area of the rings that cover the effective membrane surface area is 6.7135 cm^2 (from the total of 36 cm^2), which was considered when calculating the fluxes. The outer ring is tightly fitted to the lower sealing O-ring, ensuring stability even under intense stirring. The purpose of this design is to disrupt flow patterns and improve hydrodynamic conditions within the module, while avoiding movement or scratching of the membrane. The rings are equipped with 18 inclined baffles (45° angle, 1.4 cm height, 3 mm thickness), whose arrangement and number influence flow dynamics. *PLA*-Slim (*PLA-S*) (Fig. 1 B) adapted from the spoke-type turbulence promoter reported in Ref. [34], with the baffle-node cross-section modified to an oval (elliptical) profile to further reduce membrane contact area. Designed to reduce the contact area with the membrane, this variation limits the covered surface to only the outer annulus (3.9521 cm^2, diameter: 6.49 cm, width: 2 mm). The baffles in this design consist of 20 horizontal bands (2 mm thick) enclosing a 1.2 cm diameter annulus with a height of 2 mm. *PLA*-Thin Barrier (*PLA-TB*) (Fig. 1-C); This refinement of the PLA-UE design increases the number of baffles from 18 to 22 and reduces their thickness from 3 to 1 mm to minimize the surface area in contact with the membrane. The inner annulus is also raised to further reduce interference with the membrane surface. Polyamide dual barrier (*PA-DB*) (Fig. 1-D); Another modification of the *PLA-UE* design, this version doubles the number of baffles (from 18 to 36) while maintaining the thinner baffle design (1 mm thickness). In all cases, the effective membrane area used for the flux calculation (Equation (1)) was corrected by subtracting the promoter's membrane-contact area from the total membrane area (36 cm^2), i.e., $A_{effective} = A_{total} - A_{contact}$, following the same principle illustrated above for the

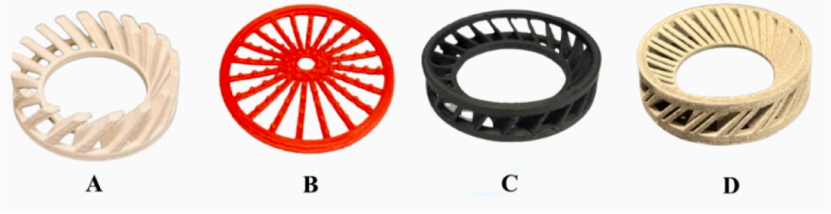


Fig. 1. Turbulence promoters designed: *PLA-UE* (A), *(B) PLA-S,* (C), *PLA-TB, and (D) PA-DB.*

PLA-UE and *PLA-S* designs.

The first three turbulence promoters were printed using fused deposition modeling (*FDM)* technology (designed with Fusion 360 software and cut in Ultimate Cure 5.0.0) on a Creality CR-10S Pro V2 3D printer (China) using polylactic acid (*PLA*) composite filament, while the fourth was made from polyamide plastic using Multi Jet Fusion (*MJF*) technology by HP Jet Fusion 5200 printer (Budapest, Hungary). The change of material for the last design was justified by the fact that by doubling the number of baffle columns, the design printed with *FDM* technology could not be properly post-treated and the supporting material could not be removed totally. So a switch to *MJF* technology was necessary, which allowed for a more complex design. FDM printing used a 0.4 mm nozzle diameter and a nozzle temperature of 215-260°C, with the complete set of slicing parameters (layer height, wall, infill, and material-specific temperature settings) summarized in Table 1.

2.4. Turbulence promoters materials

The material type has a considerable impact on the flow hydrodynamics as a result of changes in the flow's contact angle with the surface. The contact angle, which is influenced by surface energy and roughness, is crucial in controlling fluid dispersion or beading on the surface. Hydrophilic materials promote fluid flow and spread, whereas hydrophobic materials increase the contact angle and hinder flow, influencing fluid dynamics, viscosity, and surface tension forces. Therefore, selecting the appropriate promoter material is critical for improving hydrodynamic performance. Based on design experiments, the best turbulence promoter design has been chosen to investigate the effect of different materials on the filtration performance (Fig. 2-A). was made as mentioned above with *PLA*. The second promoter of turbulence (hereafter referred to as 'resin') shown in (Fig. 2-B) was printed using *SLA* technology with an Anycubic Photon S type 3D printer (China), using Anycubic Eco UV Resign material; post-processing consisted of rinsing in isopropyl alcohol followed by UV curing under controlled light exposure to complete polymerization. The third turbulence promoter (Fig. 2-C) was also printed using *FDM* technology but made of thermoplastic polyurethane (*TPU*). The fourth (Fig. 2D) was produced with *DMLS* technology, using an EOSINT M270 printer (EOS, Germany) and metal (stainless steel) material.

2.5. Ultrafiltration measurements

Each experiment was performed using freshly prepared dairy wastewater in model at the prescribed concentration ratios. The membrane support, the permeate drainage mesh, and the polymer membrane were sequentially assembled on the stainless-steel base of the filtration unit. The cylindrical glass wall was then placed onto the O-ring, followed by the installation of the cover. Membrane wetting was carried out by introducing clean water at low transmembrane pressure (0.05 MPa) for 30 min. Afterward, the pure water permeate flux of the membrane was measured. Subsequently, the residual water was drained from the unit and 100 ml of freshly homogenized feed effluent was introduced. The permeate mass was continuously monitored and recorded at predetermined time intervals using balance software. The stirring speed (n) and the transmembrane pressure (*TMP*) were set at the desired values, and the concentration process proceeded until a two-fold concentration factor was achieved, corresponding to the collection of 50 mL of permeate. Upon completion of the filtration run, the reversible polarization layer was removed from the membrane surface, repositioned in the unit, and the permeation time was measured again. The irreversible resistance was then calculated using Equation (6). Samples of the initial effluent, concentrate and permeate were collected for subsequent analysis. Physicochemical characterization was performed using standard analytical instruments: pH was measured with a Thermo Scientific Orion 5-Star Plus multifunction benchtop meter (Thermo Fisher Scientific, Massachusetts, USA); turbidity was determined using a Hach 2100N turbidimeter (Hach Company, Colorado, USA); *COD* was analyzed using a Lovibond RD 125 digestion block and a Lovibond MD 200 photometer (Tintometer Group, Dortmund, Germany); and *TDS*, electrical conductivity and salinity were measured with a portable Voltcraft Cond, TDS, Salt, KBM-90 instrument (Voltcraft, Hirschau, Germany).

Table 1
FDM 3D printing parameters used to fabricate the turbulence promoter designs (Creality CR-10S Pro V2, sliced with Ultimaker Cura v5.7.0).

Category	Parameter	Value
Quality	Layer Height	0.2 mm
Quality	Initial Layer Height	0.2 mm
Quality	Line Width (all)	0.4 mm
Walls	Wall Thickness	0.8 mm
Walls	Wall Line Count	2
Top/Bottom	Top/Bottom Thickness	0.8 mm
Top/Bottom	Top/Bottom Layers	4
Infill	Infill Density	15.0%
Infill	Infill Pattern	Cubic
Infill	Infill Line Distance	12 mm
Infill	Infill Overlap	30.0%
Material (PLA/TPU)	Printing/Build Plate Temperature	210.0°C/55.0°C

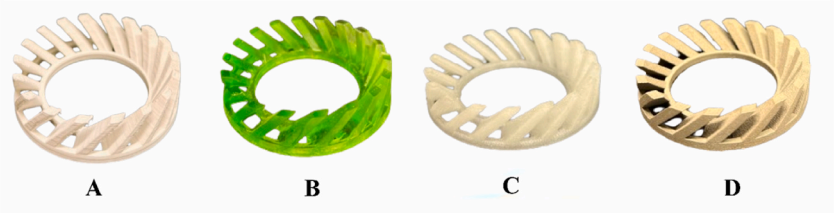


Fig. 2. Different materials of turbulence promoters: *PLA* (A), resin (B), *TPU* (C), and metal (D).

2.6. Computational fluid dynamics (CFD) model

To gain a closer understanding of the fluid dynamics of the antifouling system, a computational fluid dynamics (*CFD*) model was specified using SOLIDWORKS® Flow Simulation [41] (Fig. 3). To achieve a passive antifouling effect, it is expected that the shear stress produced by the increase in turbulence in the fluid will have a noticeable effect. However, its prediction and experimental quantification can be difficult as a result of the complexity of the filtration system. To computationally model this system, two approaches were employed: a quasi-steady state model and a time-dependent model. These approaches made it possible to efficiently predict the behavior of the system while optimizing computational cost and resources. In both cases, a 3D geometry was specified that included a cylindrical container with a capacity of 100 mL. The characteristics of the container, promoter and stirrer are in line with those described in Section 2.3. This emulates the initial volume of liquid considered in the experiments, the magnetic stirrer module, the turbulence promoter, the filter, and the mesh.

The main parameters studied were the shear stress on the filter and the surface of the promoter, the intensity of turbulence, and the turbulent energy. The velocity and pressure distribution profiles were also analyzed. To simplify the calculation, only the volume of liquid was modeled, which eliminated the requirement to specify and calculate a multiphase (air/water) system. Furthermore, the quasi-steady state model assumed continuous water flow where a pressure drop of 0.3 MPa was imposed throughout the filtration system. These adjustments allowed to simplify the mathematical model and thus minimize the calculation time. For the time-dependent model, the same characteristics from the quasi-steady state model were specified except for the rotation type model. In this case, the sliding local region model was used, which rotates the mesh and geometry within the volume, allowing a realistic simulation of the interaction of the stirrer with the fluid and the stationary domain. For the quasi-steady state, the averaging local region model was used, which is a steady-state approximation used to model rotating components without rotating the mesh. SOLIDWORKS® Flow Simulation employs a finite volume formulation on a structured Cartesian mesh (Fig. 3). The computational domain is discretized into hexahedral cells generated through an automatic meshing procedure, with local refinement applied in regions of high velocity and pressure gradients. The mesh is based on an octree subdivision approach, allowing progressive refinement of cells to accurately capture flow characteristics near solid boundaries and within complex geometric regions. This methodology allows for accurate representation of the geometry while maintaining computational efficiency in the solution of the governing transport equations.

2.6.1. Governing equations

The fluid flow across the filtration system was modeled by coupling the continuity equation (Eq. (9)) and the momentum conservation equation (Eq. (10)) [41]. In this model, the process was assumed to occur isothermally, thus energy conservation equation was not included. Flow Simulation uses the Favre-averaged Navier-Stokes equations to predict turbulent flows, which consider the time-averaged effects of the flow turbulence on the flow parameters, whereas the other (large-scale, time-dependent phenomena) are considered directly. Following this approach, extra terms known as the Reynolds stresses appear in the equations. To close this system of equations, Flow Simulation employs transport equations for the turbulent kinetic energy and its dissipation rate, the k-ε model (see Table 2 for nomenclature).

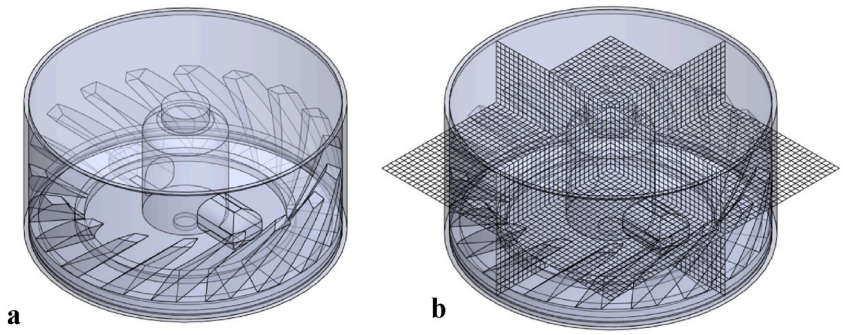


Fig. 3. (a) 3D geometry of the *CFD* model of the filtration system. (b) Computational mesh generated for the *CFD* simulation.

Table 2
Computational fluid dynamics model nomenclature.

Variable/Expression	Description
ρ	Fluid density
t	Physical time
$\underline{u}$	Flow velocity vector
p	Pressure
μ	Dynamic viscosity
$\mu_t = f_\mu \frac{C_\mu \rho k^2}{\varepsilon}$	Turbulent eddy viscosity coefficient
$f_\mu = \left[1 - \exp(-0.0165 R_y)\right]^2 \cdot \left(1 + \frac{20.5}{R_T}\right)$	Turbulent viscosity factor, where $R_T = \frac{\rho k^2}{\mu\varepsilon}$ and $R_y = \frac{\rho\sqrt{k}y}{\mu}$ and y is the distance from the wall.
$\underline{\underline{\tau}} = \mu\left(\nabla\underline{u} + (\nabla\underline{u})^T - \frac{2}{3}(\nabla\cdot\underline{u})I\right)$	Viscous shear stress tensor
$\underline{S} = \underline{S}^{porous} + \underline{S}^{gravity} + \underline{S}^{rotation}$	Mass-distributed external force per unit mass due to a porous media resistance ($\underline{S}^{porous}$), a gravity ($\underline{S}^{gravity} = \rho\underline{g}$), and the coordinate system's rotation ($\underline{S}^{rotation}$)
$\underline{\underline{\tau}}^R = \mu_t\left(\nabla\underline{u} + (\nabla\underline{u})^T - \frac{2}{3}(\nabla\cdot\underline{u})\underline{\underline{I}}\right) - \frac{2}{3}\rho k\underline{\underline{I}}$	Reynolds-stress tensor
k	Turbulent kinetic energy
ε	Turbulent dissipation rate
$S_k = \tau^R : \nabla\underline{u} - \rho\varepsilon + \mu_t P_B$	Source term of kinetic energy
$S_\varepsilon = C_{\varepsilon 1}\frac{\varepsilon}{k}(f_1\tau^R : \nabla\underline{u} + \mu_t C_B P_B) - C_{\varepsilon 2} f_2 \frac{\rho\varepsilon^2}{k}$	Source term of dissipation rate. Constant C_B is defined as: $C_B = 1$ when $P_B > 0$, and 0 otherwise. $f_1 = 1 + \left(\frac{0.05}{f_\mu}\right)^3$ and $f_2 = 1 - \exp(-R_T^2)$
$P_B = -\frac{1}{\sigma_B}\underline{g}\cdot\frac{\nabla\rho}{\rho}$	Turbulent generation due to buoyancy forces. Constant $\sigma_B = 0.9$.
$\underline{g}$	Gravitational acceleration vector
C_μ, $C_{\varepsilon 1}$, $C_{\varepsilon 2}$, σ_k, σ_ε	C_μ, $C_{\varepsilon 1}$, $C_{\varepsilon 2}$, σ_k, σ_ε are defined empirically. In Flow Simulation the following typical values are used: $C_\mu = 0.09$, $C_{\varepsilon 1} = 1.44$, $C_{\varepsilon 2} = 1.92$, $\sigma_\varepsilon = 1.3$, $\sigma_k = 1$. The parameters k and μ_t are zero for purely laminar flows.

Continuity equation

$$\frac{\partial\rho}{\partial t} + \nabla\cdot(\rho\underline{u}) = 0 \tag{9}$$

Conservation of momentum equation

$$\frac{\partial(\rho\underline{u})}{\partial t} + \nabla\cdot(\rho\underline{u}\otimes\underline{u}) + \nabla p = \nabla\cdot\left(\underline{\underline{\tau}} + \underline{\underline{\tau}}^R\right) + \underline{S} + \underline{S}_I^p \tag{10}$$

For Newtonian fluid the viscous shear stress tensor is defined using (Eq. (11)),

$$\underline{\underline{\tau}} = \mu\left(\nabla\underline{u} + (\nabla\underline{u})^T - \frac{2}{3}(\nabla\cdot\underline{u})I\right) \tag{11}$$

Following the Boussinesq assumption, the Reynolds-stress tensor has the following form (Eq. (12)),

$$\underline{\underline{\tau}}^R = \mu_t\left(\nabla\underline{u} + (\nabla\underline{u})^T - \frac{2}{3}(\nabla\cdot\underline{u})\underline{\underline{I}}\right) - \frac{2}{3}\rho k\underline{\underline{I}} \tag{12}$$

in the frame of the $k-\varepsilon$ turbulence model, μ_t is defined using two basic turbulence properties, namely, the turbulent kinetic energy k and the turbulent dissipation ε (see nomenclature Table 2).

Two additional transport equations (Eq. (13) and Eq. (14)) are used to describe the turbulent kinetic energy and dissipation.

$$\frac{\partial(\rho k)}{\partial t} + \nabla\cdot(\rho\underline{u}k) = \nabla\cdot\left[\left(\mu + \frac{\mu_t}{\sigma_k}\right)\nabla k\right] + S_k \tag{13}$$

$$\frac{\partial(\rho\varepsilon)}{\partial t} + \nabla\cdot(\rho\underline{u}\varepsilon) = \nabla\cdot\left[\left(\mu + \frac{\mu_t}{\sigma_\varepsilon}\right)\nabla\varepsilon\right] + S_\varepsilon \tag{14}$$

where S_k and S_ε are the source terms of turbulent kinetic energy and dissipation rate, respectively.

2.6.2. CFD model specification and boundary conditions

To computationally model the antifouling system, two different approaches were followed: a quasi-steady state model and a time-

dependent model. In the experiment, a specific volume of liquid is placed within the vessel and subsequently drained using a pressure difference created by an inert atmosphere. Although the process is inherently time-dependent, modeling it as such in *CFD* introduces significant computational challenges. On the one hand, a time-dependent model was selected under scenarios where knowing the position of the rotor is important, and when the fluid velocity or turbulent energy distributions across the fluid are required. The time-dependent model was simulated for a total duration of 6 s, utilizing a fixed 1 s output sampling interval. On the other hand, determining transient pressure distributions across the fluid domain and friction coefficient on the filter surfaces presents significant computational challenges. Therefore, assuming a quasi-steady state process proved to be the most practical approach for estimating these averaged flow parameters. The quasi-steady state simulation relies on the assumption that, within a discrete time interval during filtration, flow parameters such as the pressure and friction coefficient remain constant, as they would in a fully steady flow. Both approaches assume a continuous, single-phase water flow during the filtration process. This assumption significantly simplifies the analysis by eliminating the need to model a two-phase flow or track the water-air surface. Consequently, the primary boundary conditions are defined at the pressure openings, specifying a pressure drop of 0.3 MPa across the filtration system. A no-slip boundary condition was applied to the vessel and promoter walls. The filter's permeability was determined dynamically by the simulation software using an input table of empirical pressure drop vs. flow rate data, which was curve-fitted to extract the porous media resistance parameters (points at 0 MPa at 0 m^3/s, and 0.3 MPa at 1.1154×10-7 m^3/s, length 0.001 m, and porosity 0.5). The working fluid was defined as liquid water at a reference temperature of 20°C, modeled as an incompressible fluid with a constant density of 997 kg/m^3 and a dynamic viscosity of 0.001 Pa s.

For the time-dependent model, a sliding local rotating region was specified to specify the rotating domain. For the quasi-steady state model, the averaging local rotating region was selected to specify the rotating domain. In both cases, the stirrer is rotating in a clockwise direction at 400 rpm angular velocity. Sliding local rotating region is employed for calculating time-dependent (transient) flows in cases where the rotor-stator interaction is strong, when a time-accurate solution for rotor-stator interaction (rather than a time-averaged solution) is desired. On the other hand, averaging rotating region is used when only the overall performance or global behavior of the system over time is of interest, and not the exact fluctuations. It is much more economical and faster from a computational point of view.

To ensure that the numerical results are independent of spatial discretization, a mesh independence test was conducted across five refinement levels, ranging from 6940 to 377,061 elements, evaluated for four model configurations (with and without the turbulence promoter, and with and without the porous-media filter representation). The global mass flow rate imbalance between the inlet and outlet ($\Delta\dot{m}$) was used as the convergence criterion. Significant mass imbalances were observed at the two coarsest levels (6940 and 19,437 elements), but the imbalance decayed rapidly and plateaued from 52,890 elements onward, with negligible further change at 128,914 or 377,061 elements despite a substantial increase in computational cost (Fig. 4). The 52,890-element mesh was therefore selected as the working spatial resolution for all subsequent simulations, providing an adequate balance between numerical accuracy, mass conservation, and computational cost. The solver employs a fully implicit time-integration scheme, which evaluates the governing equations at the future time level and thereby maintains numerical stability over larger time intervals [42]. Building on this formulation, the software dynamically adapts the temporal discretization throughout the simulation, continuously adjusting the time-step duration based on local velocity gradients, mesh resolution, and convergence criteria, in order to capture the transient flow phenomena efficiently [41]. The 1 s value stated above therefore refers to the results output interval rather than the solver's internal time step.

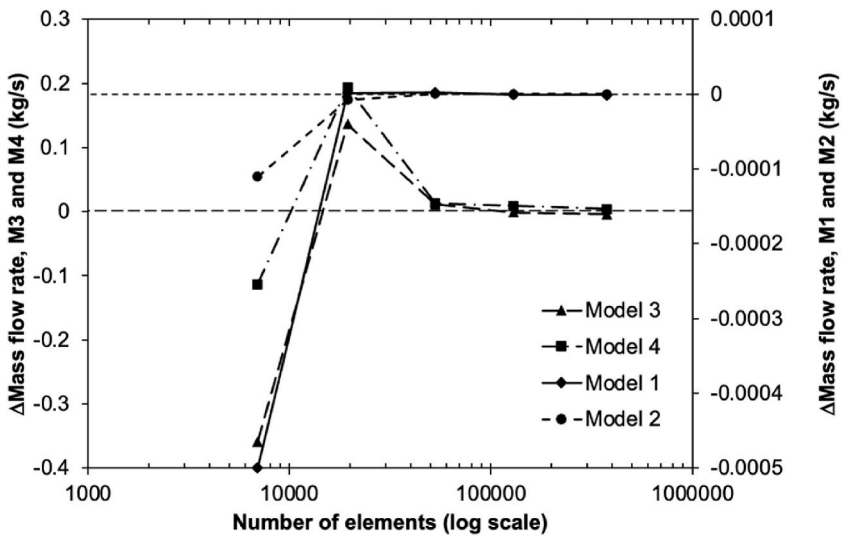


Fig. 4. Mesh independence study based on global mass flow rate imbalance ($\Delta\dot{m}$) across five spatial discretization levels.

3. Results and discussion

3.1. The effects of turbulence promoter designs on filtration parameters

Based on our preliminary study [36] A pressure of 0.3 MPa, a stirring speed of 400 rpm, and a 20 kDa *PES* membrane were fixed as operational parameters. The aim was to determine and quantify the improvement in filtration conditions under the effect of changing flow conditions using different turbulence promoter designs. The design that was found to be the most effective was used for further investigation in the next series of experiments, focusing on the effect of different materials. Four promoter designs (*PLA-UE*, *PLA-S*, *PLA-TB*, and *PLA-DB*) were used, while control measurements were also performed for comparability and repeated to ensure reproducibility.

3.1.1. Effects of turbulence promoter designs on flux values

The integration of various turbulence promoter designs into the device resulted in observed flux changes, which varied from increases to decreases. The *PLA-TB* design showed different results, where it improved the average flux by 6% in one measurement, but reduced it by 9% in another. The *PA-DB* design consistently worsened the average flux by 3% compared to the control. Both *PLA-UE* and *PLA-S* demonstrated notable improvements, with approximately 15% increases in average flux. Together, these designs exhibited the best overall performance. Fig. 5 highlights the temporal flux changes. In particular, the *PLA-S* design provided the most favorable improvement. Compared to the control, it exhibited smaller flux reductions, reduced the filtration time from 50 to 44 min, and minimized the initial flux drop. The *PLA-UE* design also performed well, with flux values and filtration times intermediate between the *PLA-S* and the control. On the contrary, the *PLA-TB* and *PA-DB* designs consistently underperformed, with average fluxes below control and filtration times increasing by 10 min. The *PA-DB*, made of polyamide, appears to be suboptimal due to material limitations. A linear trend analysis of the initial relative flux (J/J_0) confirmed that *PLA-S* had the smallest slope, indicating the least initial flux drop. The control and *PLA-UE* designs showed parallel trends, suggesting a minimal impact on the initial flux dynamics, while *PLA-TB* and *PA-DB* showed steeper declines. The *ANOVA* results (Fig. 6) indicated that *PLA-UE* and *PLA-S* outperformed the control and other designs in average flux, a trend that was consistent across both independent replicates (95% confidence level); given the limited number of independent replicates (n = 2), this result is best interpreted as a strong and consistent trend rather than a fully powered statistical confirmation. Neither the *PLA-TB* nor *PA-DB* designs showed comparable improvements over the control.

3.1.2. Effects of turbulence promoter designs on retention values

Minor differences in organic matter retention values were observed during the integration of different turbulence promoter designs, although these differences were not statistically significant. Fig. 7 shows changes of 0.7%, 3%, 4% and 7% for PA-DB, PLA-TB, PLA-S, and PLA-UE, respectively, compared to the control value. The highest COD retention was recorded for the PLA-UE design; however, this difference relative to the other designs and to the control was not statistically significant. In contrast to the substantial and consistent increase in permeate flux described above, COD retention was therefore not meaningfully affected by any of the turbulence promoter designs. This suggests that the turbulence promoters primarily reduced concentration polarization and reversible fouling,

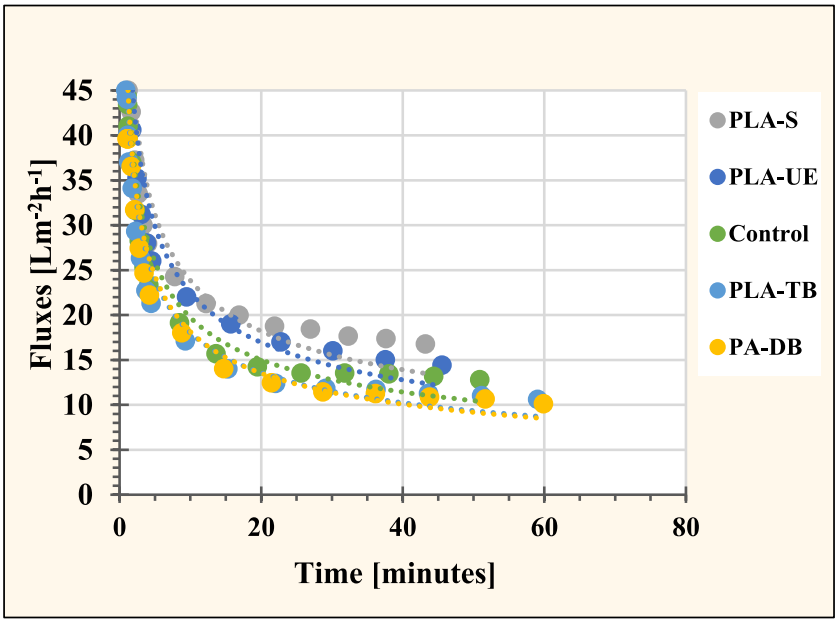


Fig. 5. Variation of permeate fluxes as a function of time with different turbulence promoters (20 kDa *UF* membrane, T = 25°C, *TMP* = 0.3 MPa, n = 400 rpm).

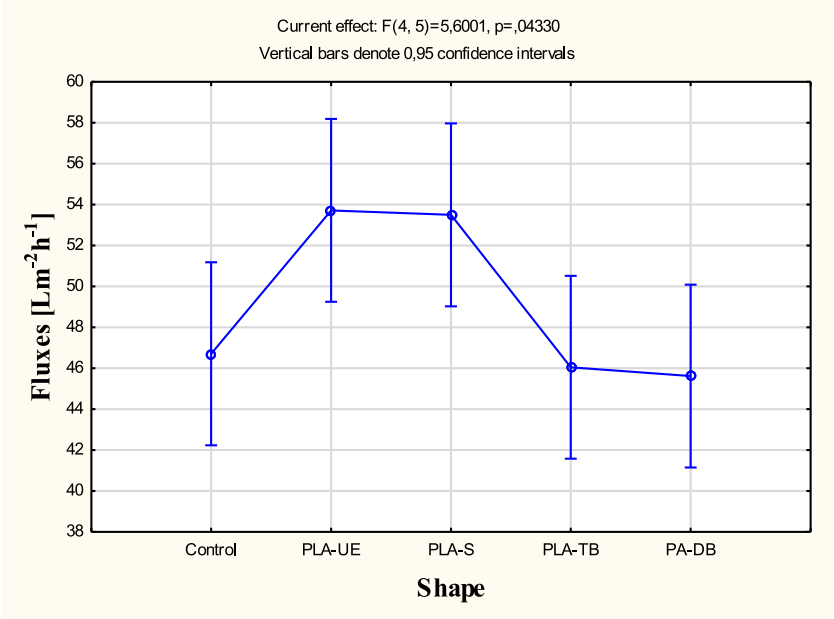


Fig. 6. Result of ANOVA: Average flux changes with different turbulence promoters.

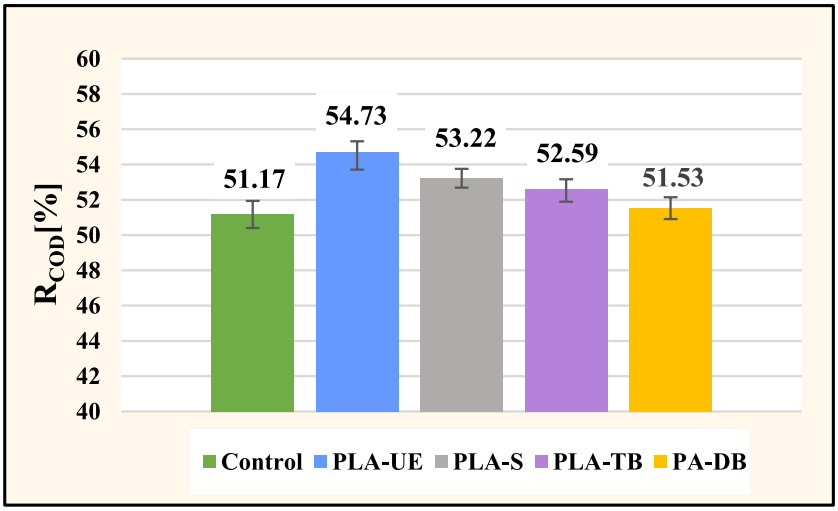


Fig. 7. Membrane retention values versus organic matter content with different turbulence promoter based on *COD* measurements (20 kDa *UF* membrane, T = 25°C, *TMP* = 0.3 MPa, n = 400 rpm).

Table 3
Raw R_T values for each turbulence promoter design, across two independent experimental replicates, and the resulting average percentage reduction relative to the control.

Condition	R_T Rep.1 [$\times 10^{13}$ m^{-1}]	R_T Rep.2 [$\times 10^{13}$ m^{-1}]	Average reduction
Control	29.74	29.74	-
PA-DB	28.84	28.73	3.2%
PLA-UE	27.19	27.40	8.2%
PLA-TB	20.25	25.72	22.7%
PLA-S	20.69	21.63	28.9%

thereby increasing flux, without altering the intrinsic selectivity of the membrane, since the membrane pore structure itself remained unchanged. Consequently, the system demonstrated higher permeability, while organic matter retention remained essentially unchanged.

3.1.3. *Effects of turbulence promoter designs on resistance values*

Consistent improvements in resistance values were observed during the design test when different designs of turbulence promoters were inserted. Each insertion caused a decrease in total resistance values. This trend was confirmed by comparative data from two independent experimental replicates (Table 3). Fig. 8 shows an average reduction in total resistance of 3.2%, 8.2%, 22.7%, and 28.9% for PA-DB, PLA-UE, PLA-TB, and PLA-S, respectively, relative to the control. On average, the total resistance to filtration was composed of 1 to 2% membrane resistance, 5-6% irreversible resistance, and 92-94% reversible resistance. Importantly, the reduction in total resistance was primarily driven by slight decreases in the reversible and irreversible resistance components, with a negligible contribution from membrane resistance. The PA-DB design showed only a marginal, non-significant change relative to the control, whereas a more substantial reduction was observed with the PLA-TB configuration, and a smaller but consistent decrease was obtained with the PLA-UE design. Most notably, the PLA-S design demonstrated the best performance among the tested designs, achieving the largest average reduction in total resistance (28.9%) across the two independent replicates. These trends were confirmed by ANOVA, with significant reductions in resistance observed for the PLA-S and PLA-TB designs in Fig. 9. A slight improvement was shown by the PLA-UE design, albeit not significant, while no meaningful overall resistance change was shown by the PA-DB design.

Beyond quantitative results, these findings help to clarify how the geometry of the turbulence promoters influences the behavior of the local flow and fouling. In general, their performance seems to depend on finding the right balance between generating enough flow disturbance and preserving enough open membrane area for effective permeation. The *PLA-S* design appears to achieve this balance most effectively, as it minimizes contact with the membrane, while introducing well-placed structural features that improve local shear and promote secondary flows without significantly blocking the surface. This helps to keep foulants away from the membrane and reduces the buildup of the reversible fouling layer, which explains the notable decrease in total resistance. The *PLA-TB* design, with thinner baffles and reduced structural interference, appears to offer a compromise by providing some enhancement in shear while limiting obstruction, leading to moderate performance gains. In comparison, the *PLA-UE* design, with its larger contact area, also improves mixing and induces vortex formation, but the increased surface coverage may partially limit permeation, resulting in a smaller overall improvement. On the other hand, the *PA-DB* design, which includes a high number of baffles, likely overcomplicates the flow field, creating localized resistance zones and disrupting beneficial recirculation, ultimately reducing the efficiency of foulant removal and explaining its relatively limited performance.

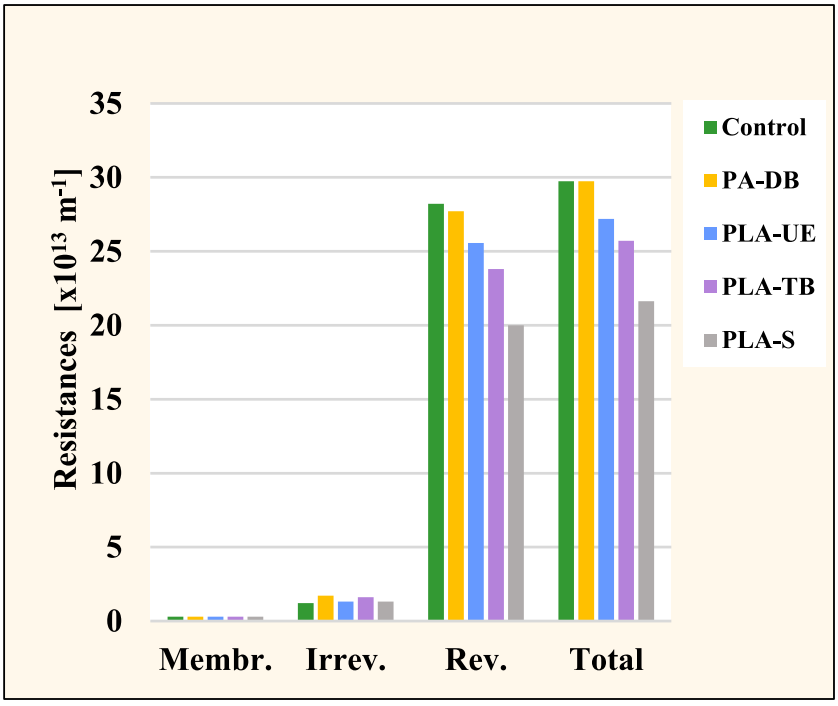


Fig. 8. Result of ANOVA: average of total resistance values with different turbulence promoter.

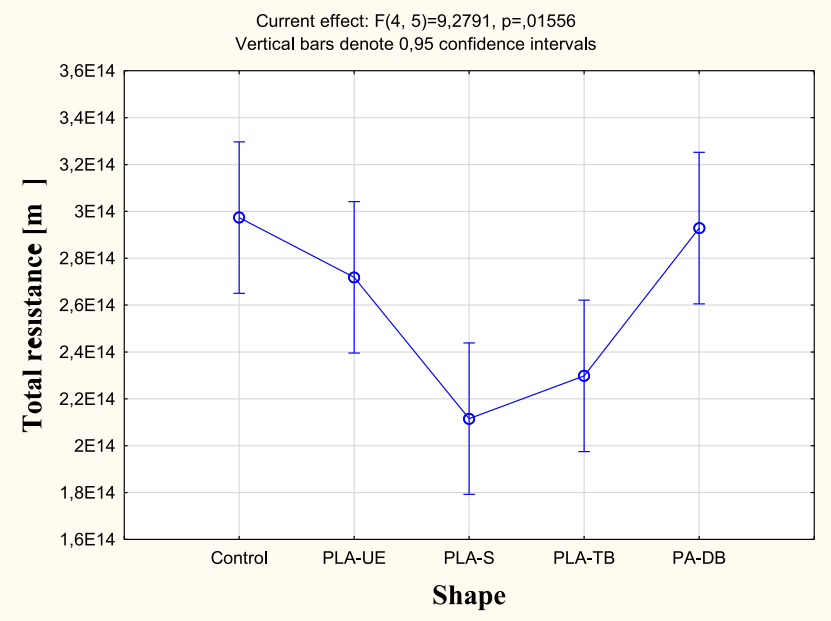


Fig. 9. Variation of resistance values with different turbulence promoter design (20 kDa UF membrane, T = 25°C, *TMP* = 0.3 MPa, n = 400 rpm).

3.2. The effects of turbulence promoter materials on filtration parameters

As a result of design measurements, a significant increase in flux values was obtained with the *PLA-UE* and *PLA-S* designs, whereas the organic matter retention was only slightly improved by all designs, with the *PLA-UE* design showing the best results. However, the total resistance value was reduced by all designs except the *PA-DB* design, but it was most significantly reduced by the *PLA-S* design. When these aspects were taken into account for materials measurements, *PLA-S* or *PLA-UE* was selected. However, since the next series of measurements aimed to use stainless steel material, the *PLA-S* design was excluded because of its excessively fine, tiny, and short parts. Consequently, the *PLA-UE* design was chosen. *TPU*, resin, and metal turbulence promoters with the same design were tested. For simplicity, *PLA-UE* will be referred to as *PLA* in subsequent discussions.

3.2.1. Effects of turbulence promoter materials on flux values

Variation in the flux values was observed during the material testing. A large increase in the average flux was observed with the insertion of all turbulence promoters. The differences in terms of material were small, but the highest average fluxes were observed with the resin. An increase of 14.58%, 16.92%, 19.44%, and 22.34% obtained by *PLA*, metal, *TPU*, and resin, respectively. Repetition of the measurements confirmed that the experimental ultrafiltration was sufficiently reproducible. Changes in the average fluxes are shown in Table 4 below.

In terms of material, significantly smaller differences were observed in the measurements compared to those obtained from the testing of different designs. Very similar results were obtained from the variations in flux values over time, as highlighted in Fig. 10. It was observed that the flattening and converging stage was reached earlier and with lower flux values in the control measurements. This indicates that with the insertion of a turbulence promoter with different materials, the initial flux values, in addition to being higher, were maintained at elevated levels for a longer duration. Furthermore, it was noted that the magnitude of the time course of the flux values was more influenced by the resinous material. A straight line was fitted to the values of the initial relative flux decrease over time to observe the trend of decrease. By the use of all of the different materials, no significant deviation in the flux-fall characteristics (linear curve) was caused compared to the control. It should be noted that these are relative or specific fluxes, that is, relative to the first measured flux value of the material itself. However, the average flux values increased with the use of all turbulence promoters. The magnitude of the initial relative flux improved by 42%, 20%, 19%, and 11.5% for resin, *TPU*, metal, and *PLA*, respectively,

Table 4
Variation of average flux values due to different materials of the *turbulence promoters*.

Turbulence promoter materials	Average flux values [$Lm^{-2}h^{-1}$]
Control	46.71
PLA	53.52
TPU	55.79
Resin	57.145
Metal	54.615

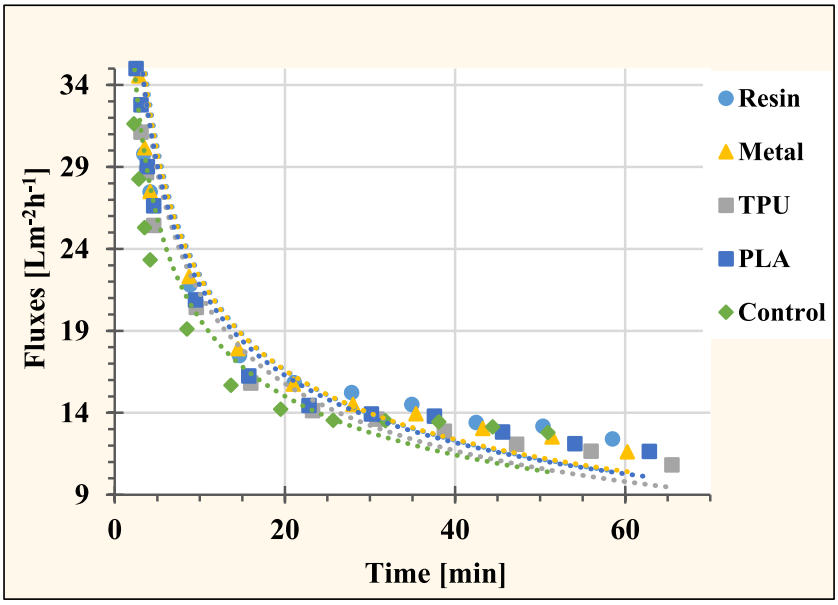


Fig. 10. Variation of permeate flux as a function of time with different material of turbulence promoters (20 kDa UF membrane, T = 25°C, *TMP* = 0.3 MPa, n = 400 rpm).

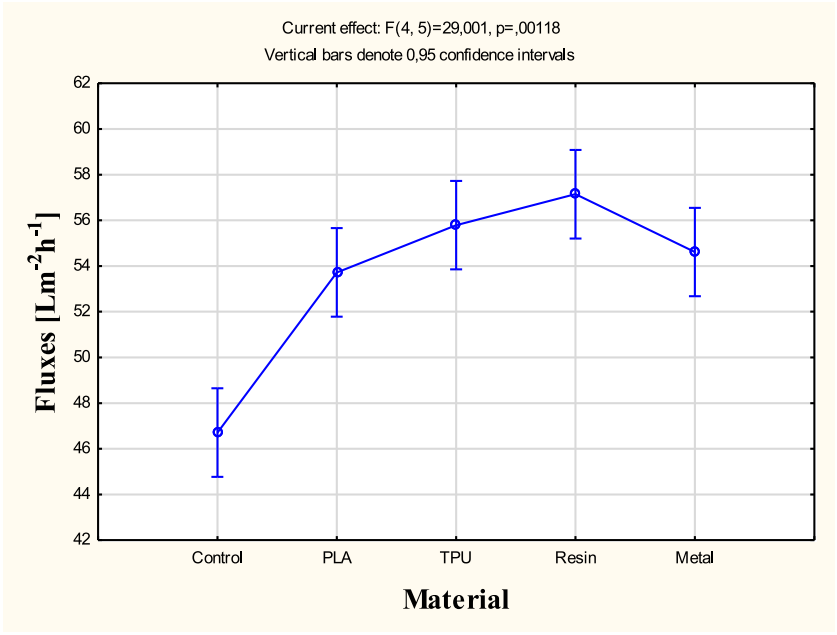


Fig. 11. Result of ANOVA: variation of average flux values with different materials of the turbulence promoters.

compared to the control. The results of ANOVA, illustrated in Fig. 11, also indicated (compared to the results of the shape analysis) a consistent difference in mean flux compared to the control (considering the confidence interval at the 0.95 level) achieved by inserting the different materials of the turbulence promoters; given the limited number of independent replicates (n = 2), this result is best interpreted as a robust trend rather than a fully powered statistical confirmation. This was expected because the most appropriate design was continued, but no meaningful differences were observed between the material designs, with the differences being small. The highest values overall were obtained by the resin.

3.2.2. Effects of turbulence promoter materials on retention values

The evolution of retention values during material testing is shown in Fig. 12. Compared with the control value (51.17%), COD

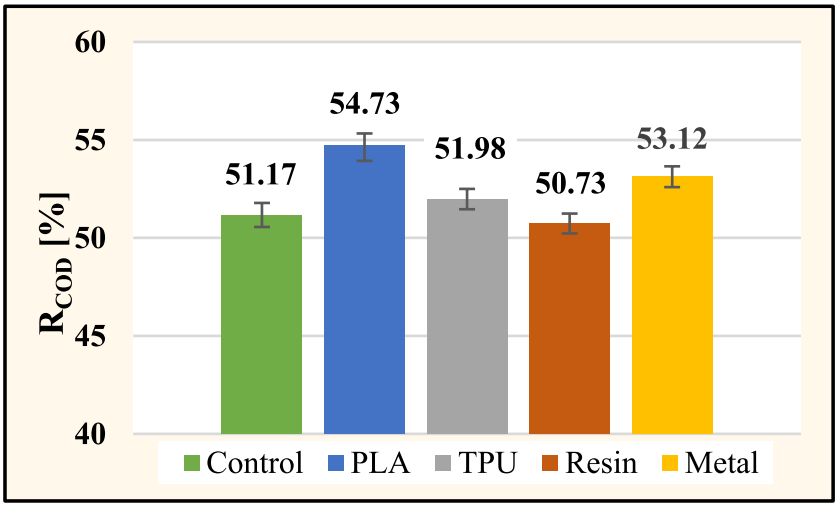


Fig. 12. Retention values for the content of organic matter (20 kDa UF membrane, T = 25°C, *TMP* = 0.3 MPa, n = 400 rpm).

retention was not consistently improved by the different turbulence promoter materials. Resin produced a slight decrease in retention (50.73%, corresponding to a change of approximately −0.9% relative to the control), rather than an improvement, while *TPU*, metal, and *PLA* showed marginal increases of 2%, 4%, and 7%, respectively. Overall, the retention of organic matter was not significantly affected by the promoter material, consistent with the turbulence promoter design results, with all measured percentage differences remaining within the range of expected experimental variability. As with the design results, this stands in contrast to the substantial and consistent increase in permeate flux achieved with all four materials, confirming that the turbulence promoters enhance filtration throughput without a significant effect on membrane selectivity.

3.2.3. *Effects of turbulence promoter materials on resistance values*

The insertion of turbulence promoters resulted in improvements in R_T values. In experiments with different materials, it was observed that insertion of the turbulence promoters led to an average increase in irreversible resistance by 1-2%, while the resulting reversible layer experienced a decrease by 1-2%. Similarly, the average distribution of total resistance was found to be 1-2% membrane, 5-6% irreversible, and 92-94% reversible resistance, as shown in Fig. 13. Again, reversible resistance played a prominent percentage role, while the intrinsic resistance of the membrane was negligible in comparison to others. However, there was a slight

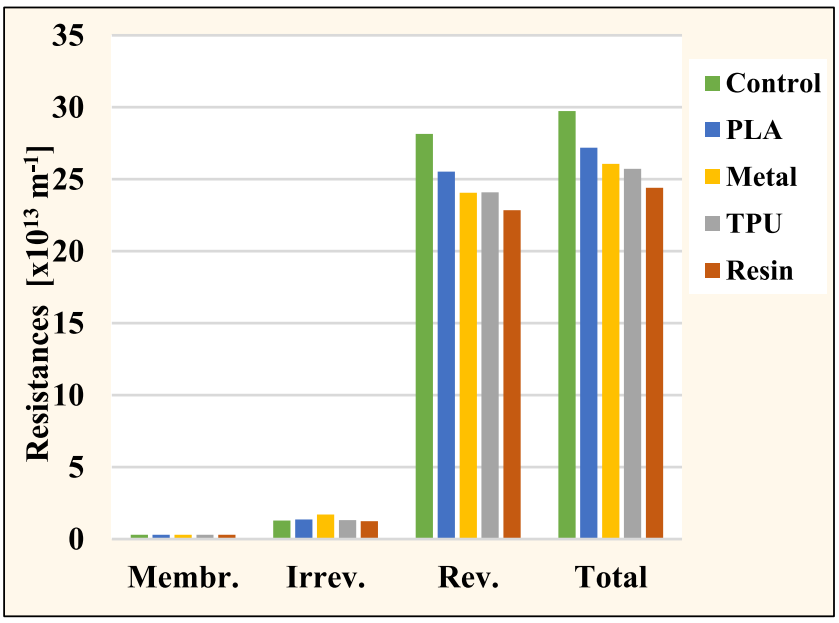


Fig. 13. Change in membrane resistance values with different turbulence promoter materials (20 kDa UF membrane, T = 25°C, *TMP* = 0.3 MPa, n = 400 rpm).

Table 5
Raw R_T values for each turbulence promoter material, across two independent experimental replicates, and the resulting average percentage reduction relative to the control.

Condition	R_T Rep.1 ($\times 10^{13}$ m^{-1})	R_T Rep.2 ($\times 10^{13}$ m^{-1})	Average reduction
Control	29.74	29.74	-
TPU	25.74	28.84	8.3%
PLA	27.19	27.24	8.5%
Metal	26.07	26.43	11.7%
Resin	24.40	24.72	17.4%

increase in the irreversible resistance, while the reversible resistance decreased. Based on the raw R_T values recalculated across two independent replicates (Table 5), total resistance decreased on average by 8.5%, 8.3%, 11.7%, and 17.4% by using *PLA*, *TPU*, metal and resin, respectively, relative to the control. However, there was an increase in irreversible resistance of 1.2% for resin, 1.5% for *PLA* and *TPU*, and 2.5% for metal. The largest decrease in resistance is shown by the resin turbulence promoter, which is significantly different from the control measurement, as indicated by the statistical analysis. In contrast, a smaller difference is observed between the metal and the *TPU* material, with a significant improvement also shown by the metal turbulence promoter.

The ANOVA for the total resistance values is illustrated in Fig. 14 (confidence interval at the 0.95 level considered). Given the limited number of independent replicates (n = 2), these results should be interpreted as consistent trends rather than fully powered statistical significance. In terms of resistances, considering the measured and calculated results together, it is observed that the resin printed material exhibits the most substantial impact, with the highest average percentage decrease in total resistance (17.4%), while the irreversible resistance experiences the lowest increase (1.2%).

3.3. Analysis of computational fluid dynamics models

Flow patterns in agitated filtration systems are complex and chaotic; thus, their description and interpretation might be limited based exclusively on experimental findings. The main objective of the *CFD* model is to describe the effects of including a turbulence promoter on the flow parameters that have a direct impact on the fluid flow through the filtration system. Fig. 15 shows the pressure distribution in the system. This figure was obtained assuming quasi-steady state, which corresponds to the initial draining stage, where the volume is the total initial volume and the stirrer is rotating at a constant angular velocity (400 rpm). As expected, the greatest pressure drop occurs across the filter and mesh due to the resistance of the porous media. When comparing the scenarios with and without the promoter, it is observed that the promoter allows a more uniform pressure distribution pattern compared to the system without a promoter. This allows a lower pressure drop in the zone not covered by the stirrer spinning area. In other words, the promoter allows for a more uniform draining, while in the scenario without the promoter a higher flow rate might be promoted by the stirrer on the circumference surface right below it.

Fig. 16 shows the velocity distribution across the axial and azimuthal planes in a time-dependent scenario for the configuration

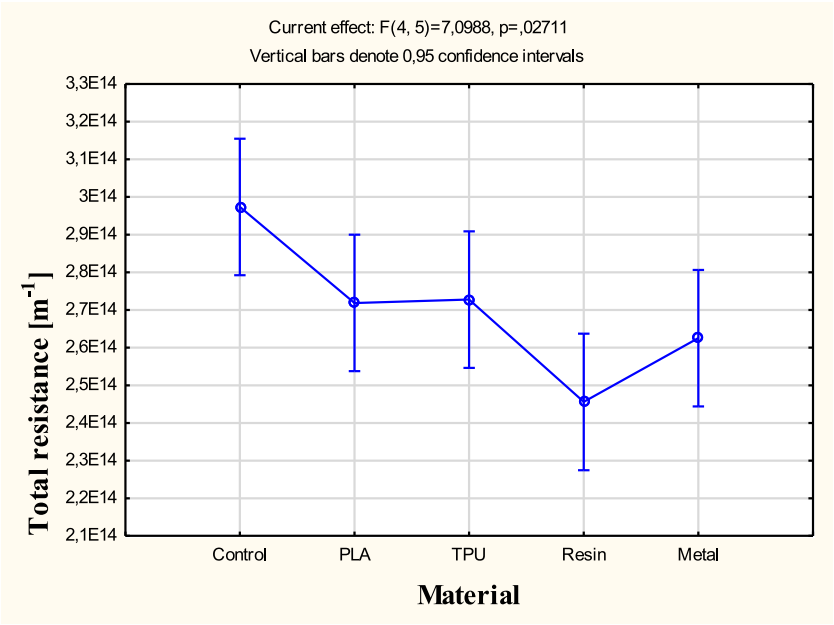


Fig. 14. Result of ANOVA: average of total resistance values with different turbulence promoter materials.

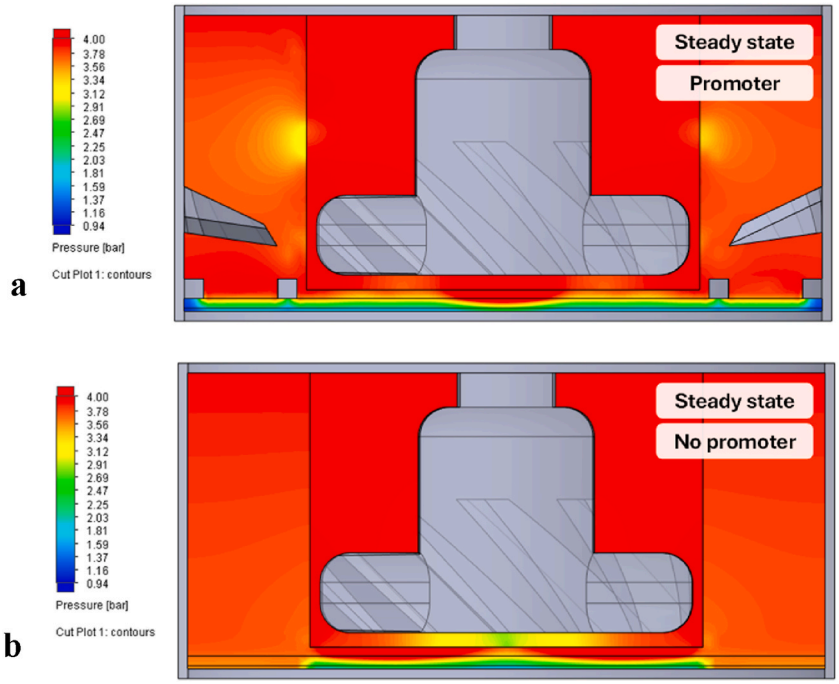


Fig. 15. Pressure distribution across the axial plane of the filtration system under quasi-steady-state conditions; (a) with the turbulence promoter and (b) without the turbulence promoter.

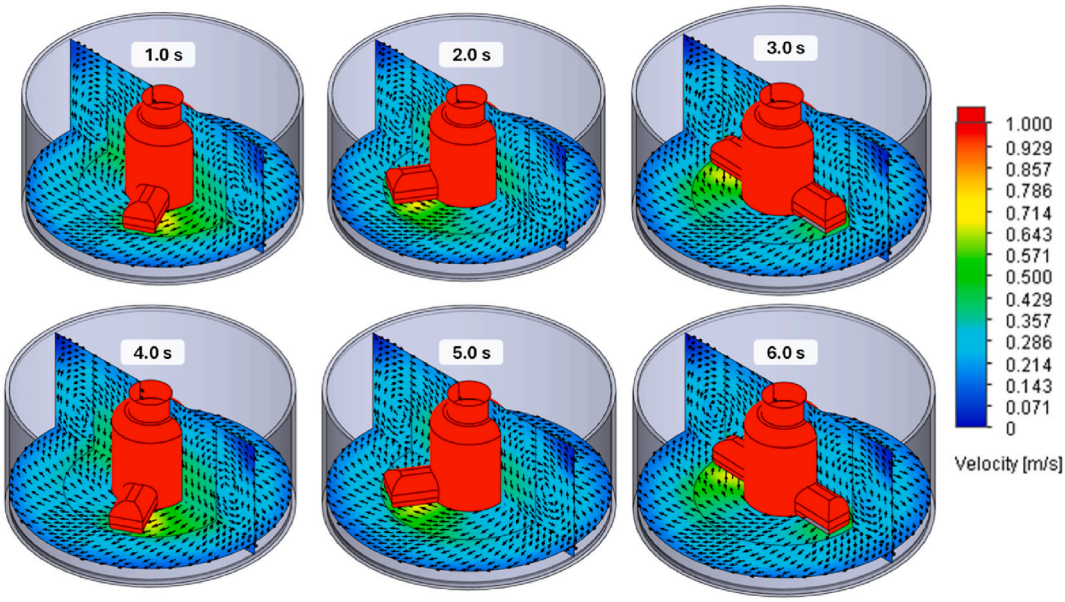


Fig. 16. Velocity distribution across the axial and azimuthal planes without a promoter.

without a promoter. The simulation spans 6 s with a 1-s output sampling interval (1.0 to 6.0 s). The time-dependent model is required to simulate the stirrer rotation (400 rpm) and the fluid-structure interaction using the sliding local region rotation model. Fluid velocity is lowest near the surface of the impeller cylinder, whereas peak velocities (~0.8 to 1.0 m/s) occur directly in front of the stirrer bulb—aligning with the theoretical impeller tip speed of 0.79 m/s. Behind the stirrer, a recirculation zone or wake is produced where the velocity is lower and local vortices are produced. Conversely, Fig. 17 shows the velocity distribution across the axial and azimuthal axes in a time-dependent scenario where the promoter is included. While the overall vector pattern remains consistent with the no promoter model, velocity magnitudes slightly decrease throughout the fluid volume, which could be driven by the presence of the

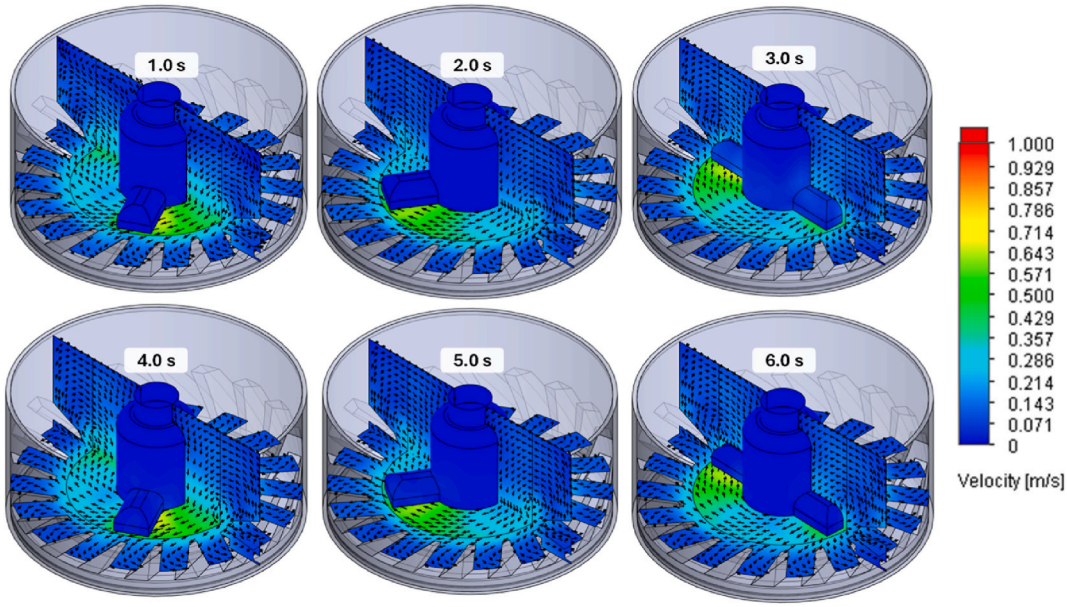


Fig. 17. Velocity distribution across the axial and azimuthal planes, including a promoter.

promoter baffles and the frictional effects rising from the fluid-structure interaction.

The skin-friction coefficient (c_f) is a dimensionless measure of the viscous drag exerted by the fluid on a solid surface. It quantifies the magnitude of the wall shear stress relative to the dynamic pressure of the fluid ($c_f = \tau_w / \left(\frac{1}{2}\rho v^2\right)$). For the quasi-steady state model with a promoter, and average friction coefficient of 0.0961 was estimated, compared to 0.0416 for the scenario without a promoter. Although the difference in average values may seem small, the inclusion of the promoter allows for maximum friction coefficient values of up to 2.8364. On the other hand, for the unmodified filtration system, the maximum was 0.3764. It is observed that, in the promoter system, the greatest friction effects are produced on the filter surface covered by the promoter blades, where the turbulence

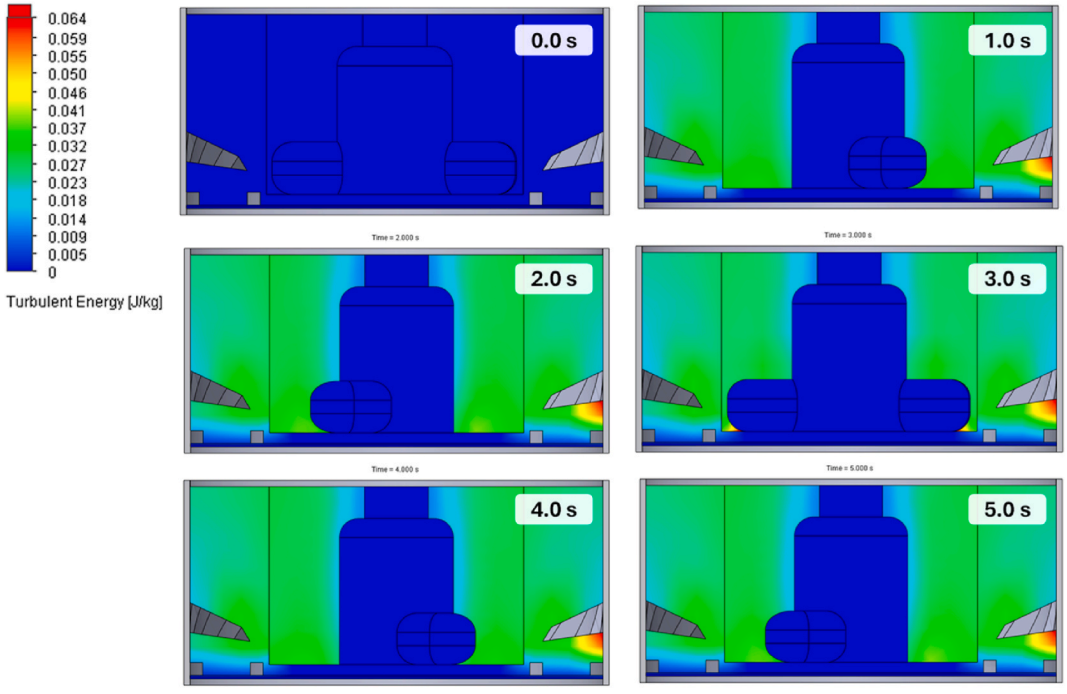


Fig. 18. Turbulent energy distribution throughout the main axis plane of the filtration system, including a promoter.

effect is expected to be highest (Fig. 18). This observation is significant since it highlights how turbulence effects promote greater friction on the filter, which in turn allows for continuous particle removal from the filter surface. In this regard, the figure shows the distribution of turbulent energy across the axial plane. The highest values are found in the fluid core and decrease significantly from the midzone toward the vessel walls and the filter surface. Notably, the highest turbulent energy occurs beneath the promoter baffles and decreases as the fluid approaches the filter wall because of the nonslip boundary condition. Although the turbulent energy is lower in the filter region beneath the promoter baffles, compared to the turbulent fluid region, this value decreases even further below the stirrer module, as previously described, leading to a lower friction coefficient on the filter surface below the stirrer module. The turbulent energy is low near the solid boundaries, primarily due to turbulence behavior in the viscous sublayer and due to the nonslip condition. The *CFD* results provide mechanistic support for the improvements observed experimentally, linking promoter geometry to increased shear stress and turbulence energy. This integrated experimental-numerical approach advances beyond prior studies that relied primarily on experimental observations or simulations alone.

4. Conclusions

This study demonstrated the effectiveness of the turbulence promoter in improving ultrafiltration performance and mitigating membrane fouling in dairy wastewater treatment. Two special configurations, the *PLA-UE* and *PLA-S* designs, substantially and consistently enhanced permeate flux, with increases of approximately 15% compared to the control. In contrast, *COD* retention was not significantly affected by either the promoter design or material; the largest observed difference (7%, with *PLA-UE*) fell within the range of experimental variability and was not statistically significant. In terms of resistance reduction, *PLA-S* exhibited the most substantial improvement, decreasing total resistance by 28.9%. Material selection further influenced filtration efficiency, with the resin turbulence promoter leading to a 22.3% increase in flux and a 17.4% reduction in total resistance. *TPU* and metal materials also showed notable improvements, increasing the flux by 19.4% and 16.9%, respectively. Statistical analyses were consistent with these findings, indicating that turbulence promoters effectively enhance hydrodynamic conditions within the membrane module, although the limited number of independent replicates ($n = 2$ per condition) warrants cautious interpretation of formal statistical significance. Finally, *CFD* simulations allow for a closer view of the hydrodynamic behavior of the filtration system, demonstrating that the shear stress on the filter surface becomes greater when the turbulence promoters are included.

CRediT authorship contribution statement

Aws N. Al-Tayawi: Writing – review & editing, Writing – original draft, Visualization, Validation, Software, Resources, Methodology, Investigation, Formal analysis, Data curation, Conceptualization. **Zsuzsanna Horváth Hovorka:** Writing – review & editing, Writing – original draft, Visualization, Validation, Software, Methodology, Investigation, Formal analysis, Data curation. **Orlando Castilleja-Escobedo:** Writing – review & editing, Writing – original draft, Visualization, Validation, Software, Methodology, Investigation, Formal analysis, Data curation, Conceptualization. **David De Haro Del Rio:** Writing – review & editing, Writing – original draft, Visualization, Validation, Software, Methodology, Investigation, Formal analysis. **José L. López-Salinas:** Writing – review & editing, Visualization, Validation, Software, Resources, Methodology, Investigation, Formal analysis, Data curation. **Szabolcs Kertész:** Writing – review & editing, Validation, Supervision, Resources, Project administration, Methodology, Investigation, Funding acquisition, Data curation, Conceptualization.

Data availability

Data will be made available on request. For requesting data, please write to the corresponding author.

Declaration of competing interest

The authors declare that they have no known competing financial interests or personal relationships that could have appeared to influence the work reported in this paper.

Acknowledgements

This study was supported by the 142414 FK and 2022-1.2.6-TÉT-IPARI-TR-2022-00011 grants from the National Research, Development and Innovation Office (NKFI), Hungary. Aws N. Al-Tayawi acknowledges the financial support provided through the Ministry of Culture and Innovation Research Fellowship Program, funded by the National Fund for Research, Development and Innovation (grant number EKÖP-24-3-SZTE-476). We also thank the University of Szeged Open Access Fund (8184) for support.

References

[1] M.K. Joy, D.A. Rankin, L. Wöhler, P. Boyce, A. Canning, K.J. Foote, P.M. McNie, The grey water footprint of milk due to nitrate leaching from dairy farms in Canterbury, New Zealand, Australas. J. Environ. Manag. 29 (2022) 177–199.
[2] W. Musie, G. Gonfa, Fresh water resource, scarcity, water salinity challenges and possible remedies: a review, Heliyon 9 (2023) e18685.
[3] A.S. Stasinakis, P. Charalambous, I. Vyrides, Dairy wastewater management in EU: produced amounts, existing legislation, applied treatment processes and future challenges, J. Environ. Manag. 303 (2022) 114152.

[4] H. Faraj, A. Jamrah, S. Al-Omari, T.M. Al-Zghoul, Optimization of an electrocoagulation-assisted adsorption treatment system for dairy wastewater, Case Stud. Chem. Environ. Eng. (2023) 100574.
[5] L.K.S. Lima, L.N.L. Santana, H.L. Lira, M.A. Rodríguez, M.Y.M. Souza, M.G.S. Júnior, B.S. Lira, Development of asymmetric ceramic membranes for dairy wastewater treatment–A comparison between co-sintering and conventional firing process, J. Water Process Eng. 57 (2024) 104611.
[6] M. Reig, X. Vecino, J.L. Cortina, Use of membrane technologies in dairy industry: an overview, Foods 10 (2021) 2768, https://doi.org/10.3390/foods10112768. (Accessed 8 November 2022).
[7] C.F. Bennani, B. Ousji, D.J. Ennigrou, Reclamation of dairy wastewater using ultrafiltration process, Desalination Water Treat. 55 (2015) 297–303.
[8] E.S. Mansor, E.A. Ali, A.M. Shaban, Tight ultrafiltration polyethersulfone membrane for cheese whey wastewater treatment, Chem. Eng. J. 407 (2021) 127175.
[9] L.N. Nthunya, M.F. Bopape, O.T. Mahlangu, B.B. Mamba, B. Van der Bruggen, C.A. Quist-Jensen, H. Richards, Fouling, performance and cost analysis of membrane-based water desalination technologies: a critical review, J. Environ. Manag. 301 (2022) 113922.
[10] B. Zhang, X. Feng, Assessment of pervaporative concentration of dairy solutions vs ultrafiltration, nanofiltration and reverse osmosis, Sep. Purif. Technol. 292 (2022) 120990.
[11] A.V. Bildyukevich, T.V. Plisko, F. Lipnizki, S.A. Pratsenko, Correlation between membrane surface properties, polymer nature and fouling in skim milk ultrafiltration, Colloids Surfaces a Physicochem. Eng. Asp. 605 (2020) 125387.
[12] S. Mazinani, A. Al-Shimmery, Y.M.J. Chew, D. Mattia, 3D printed fouling-resistant composite membranes, ACS Appl. Mater. Interfaces 11 (2019) 26373–26383, https://doi.org/10.1021/acsami.9b07764.
[13] S.B. Khan, S. Irfan, S.S. Lam, X. Sun, S. Chen, 3D printed nanofiltration membrane technology for waste water distillation, J. Water Process Eng. 49 (2022) 102958.
[14] N. Bhattacharjee, A. Urrios, S. Kang, A. Folch, The upcoming 3D-printing revolution in microfluidics, Lab Chip 16 (2016) 1720–1742.
[15] Z. Liu, Y. Wang, B. Wu, C. Cui, Y. Guo, C. Yan, A critical review of fused deposition modeling 3D printing technology in manufacturing polylactic acid parts, Int. J. Adv. Manuf. Technol. 102 (2019) 2877–2889.
[16] A. Khalil, F.E. Ahmed, R. Hashaikeh, N. Hilal, scp>3D</Scp> printed electrically conductive interdigitated spacer on ultrafiltration membrane for electrolytic cleaning and chlorination, J. Appl. Polym. Sci. 139 (2022), https://doi.org/10.1002/app.52292.
[17] W. Lin, Q. Wang, L. Sun, D. Wang, J. Cabrera, D. Li, L. Hu, G. Jiang, X. Wang, X. Huang, The critical role of feed spacer channel porosity in membrane biofouling: insights and implications, J. Membr. Sci. 649 (2022) 120395, https://doi.org/10.1016/j.memsci.2022.120395.
[18] K. Baitalow, D. Wypysek, M. Leuthold, S. Weisshaar, J. Lölsberg, M. Wessling, A mini-module with built-in spacers for high-throughput ultrafiltration, J. Membr. Sci. 637 (2021) 119602.
[19] Y. Ibrahim, N. Hilal, Integration of porous and permeable poly(ether sulfone) feed spacer onto membrane surfaces via direct 3D printing, Acs Appl. Eng. Mater. 2 (2024) 1094–1109, https://doi.org/10.1021/acsaenm.4c00086.
[20] B. Gu, C.S. Adjiman, X.Y. Xu, The effect of feed spacer geometry on membrane performance and concentration polarisation based on 3D CFD simulations, J. Membr. Sci. 527 (2017) 78–91, https://doi.org/10.1016/j.memsci.2016.12.058.
[21] S. Kerdi, A. Qamar, J.S. Vrouwenvelder, N. Ghaffour, Fouling resilient perforated feed spacers for membrane filtration, Water Res. 140 (2018) 211–219.
[22] A. Khalil, L. Francis, R. Hashaikeh, N. Hilal, 3D printed membrane-integrated spacers for enhanced antifouling in ultrafiltration, J. Appl. Polym. Sci. 139 (2022), https://doi.org/10.1002/app.53019.
[23] W.S. Tan, S.R. Suwarno, J. An, C.K. Chua, A.G. Fane, T.H. Chong, Comparison of solid, liquid and powder forms of 3D printing techniques in membrane spacer fabrication, J. Membr. Sci. 537 (2017) 283–296, https://doi.org/10.1016/j.memsci.2017.05.037.
[24] S. Park, Y. Dal Jeong, J.H. Lee, J. Kim, K. Jeong, K.H. Cho, 3D printed honeycomb-shaped feed channel spacer for membrane fouling mitigation in nanofiltration, J. Membr. Sci. 620 (2021) 118665.
[25] X. Qian, M. Ostwal, A. Asatekin, G.M. Geise, Z.P. Smith, W.A. Phillip, R.P. Lively, J.R. McCutcheon, A critical review and commentary on recent progress of additive manufacturing and its impact on membrane technology, J. Membr. Sci. (2021) 120041.
[26] S. Armbruster, O. Cheong, J. Lölsberg, S. Popovic, S. Yüce, M. Wessling, Fouling mitigation in tubular membranes by 3D-printed turbulence promoters, J. Membr. Sci. 554 (2018) 156–163.
[27] E. Fodor, Z. Šereš, G. Gergely, C. Hodúr, S. Kertész, Investigation of ultrafiltration parameters of different organic load wastewater types, Analecta Tech. Szeged. 16 (2022) 129–135.
[28] B. Jiang, B. Hu, N. Yang, L. Zhang, Y. Sun, X. Xiao, Study of turbulence promoters in prolonging membrane life, Membranes 11 (2021) 268.
[29] B. Wu, Y. Zhang, Z. Mao, W.S. Tan, Y.Z. Tan, J.W. Chew, T.H. Chong, A.G. Fane, Spacer vibration for fouling control of submerged flat sheet membranes, Sep. Purif. Technol. 210 (2019) 719–728, https://doi.org/10.1016/j.seppur.2018.08.062.
[30] E.H.C. Castillo, N. Thomas, O. Al-Ketan, R. Rowshan, R.K. Abu Al-Rub, L.D. Nghiem, S. Vigneswaran, H.A. Arafat, G. Naidu, 3D printed spacers for organic fouling mitigation in membrane distillation, J. Membr. Sci. 581 (2019) 331–343, https://doi.org/10.1016/j.memsci.2019.03.040.
[31] H.-Y. Tsai, A. Huang, Y.-L. Luo, T.-Y. Hsu, C.-H. Chen, K.-J. Hwang, C.-D. Ho, K.-L. Tung, 3D printing design of turbulence promoters in a cross-flow microfiltration system for fine particles removal, J. Membr. Sci. 573 (2019) 647–656, https://doi.org/10.1016/j.memsci.2018.11.081. (Accessed 8 November 2022).
[32] V.H. Ng, C.H. Koo, W.C. Chong, J.Y. Tey, Progress of 3D printed feed spacers for membrane filtration, Mater. Today Proc. 46 (2021) 2070–2077.
[33] A.N. Al-Tayawi, N.S. Gulyás, G. Gergely, Á.F. Fazekas, B. Szegedi, C. Hodúr, J.R. Lennert, S. Kertész, Enhancing ultrafiltration performance for dairy wastewater treatment using a 3D printed turbulence promoter, Environ. Sci. Pollut. Res. (2023) 1–10.
[34] N. Szpisják-Gulyás, Z. László, S. Kertész, C. Hodúr, Effects of a 3D-Printed turbulence promoter on membrane fouling during the ultrafiltration of dairy wastewater, Dairy 5 (2024) 842–861, https://doi.org/10.3390/dairy5040061.
[35] B.S. Shete, N.P. Shinkar, Dairy industry wastewater sources, characteristics & its effects on environment, Int. J. Curr. Eng. Technol. 3 (2013) 1611–1615.
[36] A. Altayawi, H. Csott, Z.H. Hovorka, I. Hatos, Z. László, G. Veréb, M. Nikola, Z. Šereš, S. Kertész, Optimization of operational parameters to enhance ultrafiltration efficiency using dairy wastewater model, Analecta Tech. Szeged. 19 (2025) 45–58.
[37] R.W. Field, J.J. Wu, Permeate flux in ultrafiltration processes—Understandings and misunderstandings, Membranes 12 (2022) 187.
[38] C. Quezada, H. Estay, A. Cassano, E. Troncoso, R. Ruby-Figueroa, Prediction of permeate flux in ultrafiltration processes: a review of modeling approaches, Membranes 11 (2021) 368.
[39] Y.O. Raji, M.H.D. Othman, N.A.H.M. Nordin, M.R. Adam, K.A.M. Said, K.A. Abdulyekeen, A.F. Ismail, M.A. Rahman, J. Jaafar, S.A. Bakar, Optimization of a high-performance poly(diallyl dimethylammonium Chloride)-Alumina-Perfluorooctanoate intercalated ultrafiltration membrane for treating emulsified oily wastewater via response surface methodology approach, Membranes 11 (2021) 956, https://doi.org/10.3390/membranes11120956.
[40] A. Kumar, U. Panda, Microfluidics-based devices and their role on point-of-care testing. Biosens. Based Adv. Cancer Diagnostics, Elsevier, 2022, pp. 197–224.
[41] Dassault Systèmes, SOLIDWORKS Flow Simulation: Technical Reference, SOLIDWORKS Help, 2025. Available within SOLIDWORKS Flow Simulation software.
[42] H.K. Versteeg, An Introduction to Computational Fluid Dynamics the Finite Volume Method, 2/E, Pearson Education India, 2007.